ADVANCED MATERIALS TECHNOLOGIES
www.advmattechnol.de

Bioinspired Ultrasensitive and Flexible Airflow Sensor based on Short Carbon Fiber Network

Chen Shen, Shuai Sun, Hui Zhang, and Zhong Zhang**

Electronic skin or wearable electronics have attached great attention due to their huge potential applications, and flexible airflow sensor, as an important part, reveals extensive applications. However, finding an efficient, low-cost, and room-temperature operation condition method to prepare flexible airflow sensors with high sensing performance still remains a challenge. Herein, inspired by filiform hairs of insects, a highly sensitive, stable, and flexible airflow sensor based on short carbon fiber network (SCFN) structure via electrostatic flocking is developed. The fabricated SCFN is endowed with an ultralow detection limit (0.053 m s^{-1}), wide detection range (0.053–2.66 m s^{-1}), multiangle response (0°–90°) with a fast response (1.7 s) and recovery time (3.4 s), together with excellent stability. Besides, its sensing mechanism is elaborated and demonstrated from microscale. Furthermore, it is applied to detect the velocity and direction of airflow through a 3D layout decoration of sensors and integrated into monitoring the leak location in a sealed reaction device. The combination of mild high-throughput preparation and high sensing performance of SCFN airflow sensor shows significant potentials in electronic skin or wearable electronics filed.

1. Introduction

Evoked by the idea of constructing a human–computer interaction world, the electronic skin or wearable electronics get rapid development in recent years.[1] Plenty of novel sensors that are able to perceive different signals in environment are urgently needed. At the same time, these novel sensors also require flexibility, miniaturization as well as simple fabrication for large-scale utilization,[2–4] quite different with the conventionally rigid and cumbersome sensors.[5–8]

Compared to pressure,[9–14] temperature,[15,16] humidity sensors,[6,17–22] reported in literature, the flexible airflow sensors are less investigated, even though they play an essential role in above applications, such as detection of gas,[23] breath monitoring,[24–26] weather observation,[27] or even monitoring of gas leakage.[28] In general, the working mechanism for the airflow sensors is based on the signal change of piezoresistive,[11,20,21,29,30] capacitive,[31,32] piezoelectric,[33–35] optical,[6,36,37] or magnetic[38] airflow-induced mechanical deformation. Occasionally, airflow-induced temperature variation[39] is also utilized for designing the airflow sensor.

So far, there are still some drawbacks for the present airflow sensors. First, many present fabrication methods are complicated, inefficient, and expensive, impractical for the large-scale production. Second, most of the airflow sensors, due to their elaborate micro/nanostructures, could not work well in complex and changeable environment. Third, many airflow sensors are lack of flexibility. Therefore, it remains a challenge to find an efficient, low-cost, and room-temperature operation condition method to prepare flexible airflow sensors with ultralow detection limit, fast response, stable, and long-term service life.

Many insects in nature have developed hair-like sensors after long evolution for perceiving surrounding information,[40–43] e.g., the cerci of crickets,[44] the fluff on spiders' legs,[45] or even filiform hairs of cockroaches.[46] They used filiform hairs serving as windows to environment, the hair-like sensors provide insects with relevant information of escape, defense, or predation. Such an ingenious and effective sensory system of insects inspired researchers to design ultrasensitive airflow sensor based on tiny hair-like structures. Herein, mimicking the filiform hair of insects, we developed a novel strategy to design an ultrasensitive and flexible airflow sensor based on short carbon fiber network (SCFN) using electrostatic flocking technique. The SCFN airflow sensor operated on the basis of piezoresistive effect. Namely, the short carbon fibers, similar to filiform hair, can be bent and swung by airflow (a force of several micro-Newtons), thus making the contact resistance of SCFN change easily. This SCFN airflow sensor exhibited excellent sensing performance, very good flexibility, remarkable abrasive resistance, and high sensing cycle stability. We fully took advantage of designability of the SCFN airflow sensor to position leakage point for a sealed space, and able to detect the

C. Shen, S. Sun, H. Zhang, Z. Zhang
CAS Key Laboratory of Nanosystem and Hierarchical Fabrication
CAS Center for Excellence in Nanoscience
National Center for Nanoscience and Technology
Beijing 100190, China
E-mail: zhangh@nanoctr.cn; zhongzhang@nanoctr.cn
C. Shen, S. Sun, H. Zhang
University of Chinese Academy of Sciences
Beijing 100049, China
Z. Zhang
CAS Key Laboratory of Mechanical Behavior and Design of Materials
Department of Modern Mechanics
University of Science and Technology of China
Hefei 230027, China

The ORCID identification number(s) for the author(s) of this article can be found under https://doi.org/10.1002/admt.202200571.

DOI: 10.1002/admt.202200571

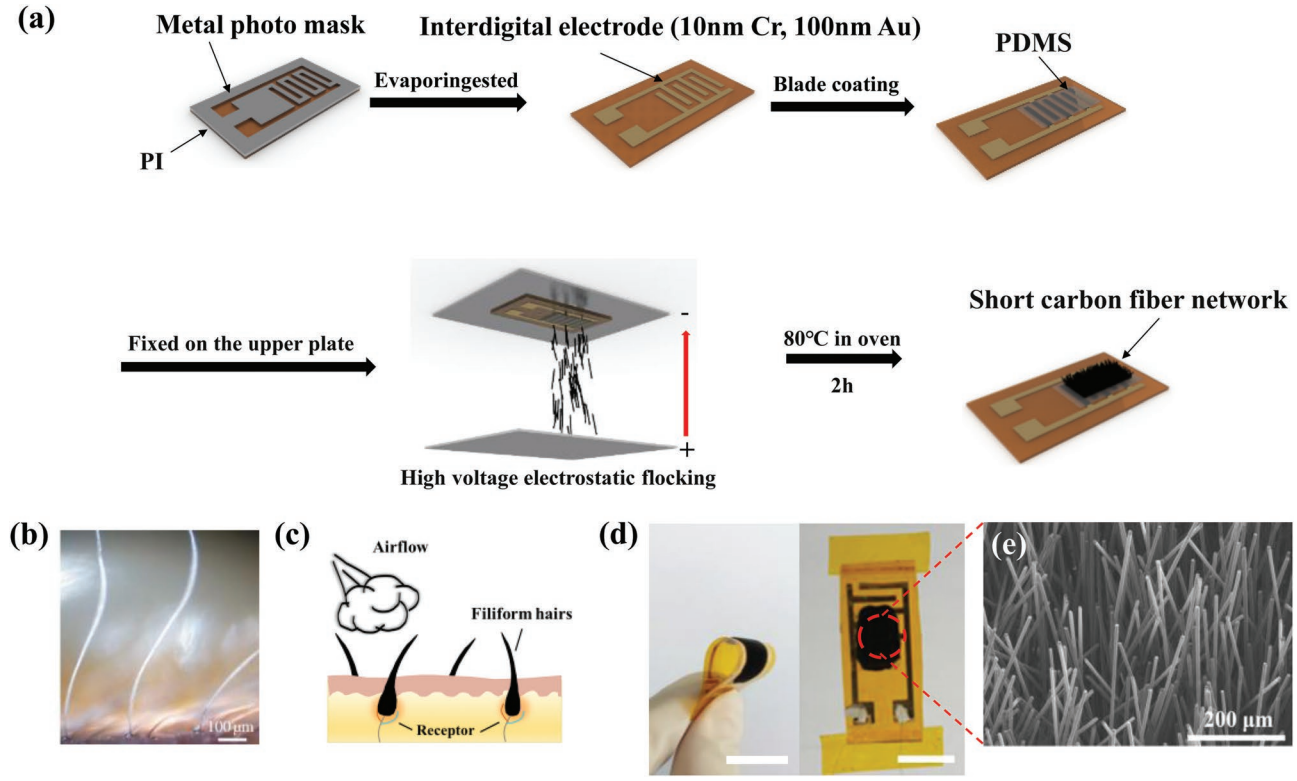

Figure 1. a) The fabrication process of SCFN airflow sensor; b) optical image of trichobothria on spider's walking leg;[47] c) schematic diagram of filiform hairs under airflow. d) Optical image of an SCFN airflow sensor (scale bar, 1 cm). e) SEM image showing the micromorphology of SCFN.

airflow direction when 3D layout decoration was employed. The excellent sensing performance of SCFN airflow sensor, along with their simple fabrication process, offers great promise for a wide application potential in electronic skin, wearable electronics, and other applications.

2. Results and Discussion

2.1. The Fabrication Principle and Process of SCFN Airflow Sensor

The fabrication process of SCFN airflow sensor is illustrated in **Figure 1**a (see details in the Experimental Section). Briefly, the SCFN airflow sensor is composed of polyimide (PI) foil, interdigital electrode, polydimethylsiloxane (PDMS) adhesive layer, and quasi-vertical short carbon fiber network from bottom to top. First, the PI foil and PDMS adhesive layer were selected due to their flexibility and stability, which make the interdigital electrode flexible and stable under constant bending and compressing. The interdigitated electrodes are prepared by a thermal evaporation process. And the electrostatic flocking technique was used to prepare a microstructure of carbon fibers (CFs) on an interdigital electrode. The methods of preparing SCFN and interdigital electrodes are mature and low-cost, which can be able to prepare in mild operating conditions. Besides, the substrate could be made into PI tape, which can be adhered to anywhere we need. Full-flexible design and mild preparation endow SCFN airflow sensor with great flexibility (Figure 1d), miniaturization, and the possibility for large-scale fabrication.

Insects construct ultrasensitive sensory system based on their tiny hairs (Figure 1b): A common characteristic of all these hair-like airflow sensors of insects is their small size and the tiny mass, just like a lever arm, these tiny filiform hairs grown on body surface can sensitively be deflected under the viscous forces exerted even by the slightest whiff of air, and then the nerves receptor under the body surface recognizes the mechanical signals to sense the airflow (Figure 1c). The resulting structure of SCFN is similar to filiform hairs of insects, which possesses a hair-like microstructure (Figure 1e). It can be observed from the situ-optical microscope (as shown in Video S1, Supporting Information) that the fibers possess similar response to filiform hairs of insects under airflow: CFs was bended and swung under the action of airflow. We chose PDMS with a smaller modulus after curing (Figure S1, Supporting Information) to build a softer "skin," which is beneficial to fibers' deformation under airflow. Too thick adhesive is avoided, because the fiber cannot penetrate through the thick adhesive and contact the metal electrodes, as a result, the conductive loop cannot be formed (Figure S2, Supporting Information). By trial and error, the PDMS thickness is set to ≈15 μm.

2.2. The Morphology and Structure of SCFN

Figure 2 reveals micromorphology of SCFN prepared with average CFs length of 508, 319, and 120 μm (Figure 2a1–a3 and Figure S3a, Supporting Information) after sieving by screen with different meshes, respectively, which are labeled as SCFN-500, SCFN-300, SCFN-100 for simplify. In general, the quasi-vertical

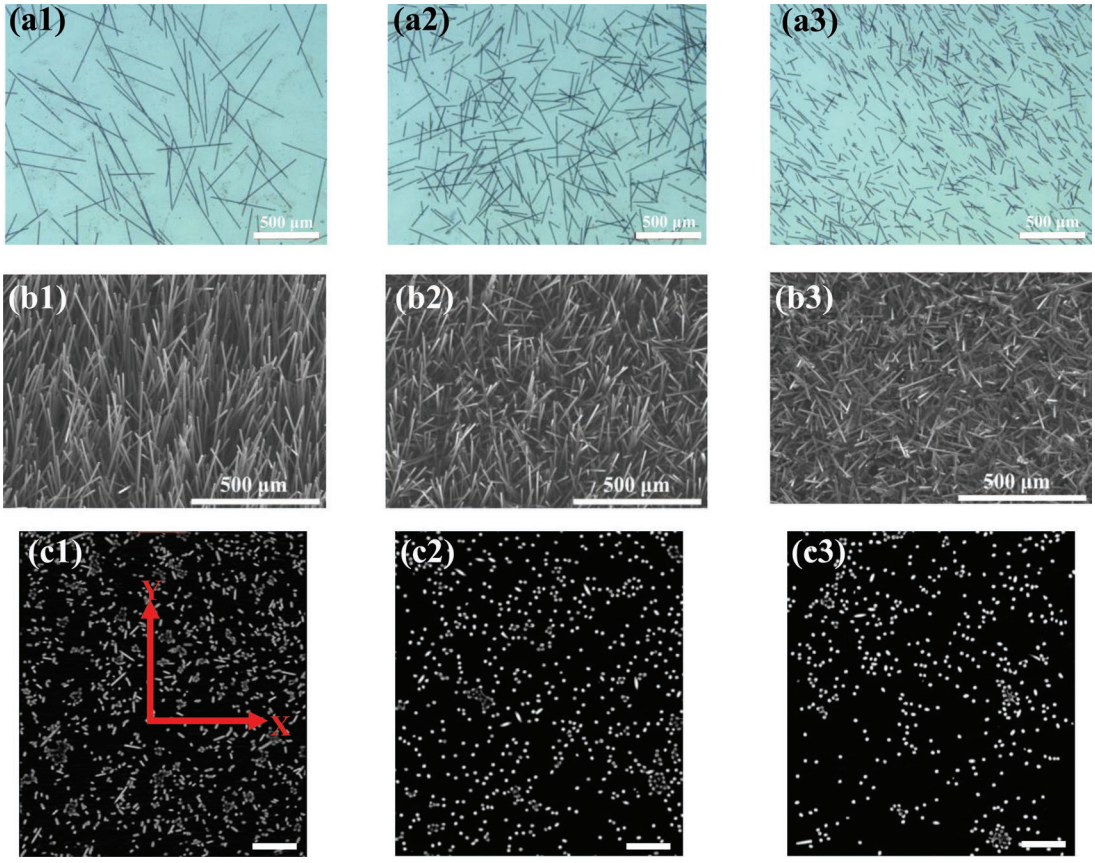

Figure 2. a1–a3) Optical images, b1–b3) SEM top view images, and c1–c3) micro-CT slice images (scale bar, 100 μm) of carbon fibers with average length around 508, 319, 120 μm. The slices were taken at the middle height of SCFN structure from the bottom of substrate (scale bar is 100 μm).

CFs contact with each other and form a conductive network in plane direction. It can be seen that the average orientation angle (Figure S3b,c, Supporting Information) decreases with decreasing fiber length. This quasi-vertical orientation of CFs is caused by the polarization on the plate electrode and the damping motion in air of short carbon fibers, within a high-voltage electric intensity (Figures S4 and S5 and Videos S2 and S3, Supporting Information). Longer CFs are easier to orient in high-voltage electric intensity[48] and form more vertical array structure than network structure (Figure 2b). In other words, short fibers are easier to contact with each other when we got a poorer oriented structure (the orientation angle is relatively small[49]). Meanwhile, we used the high electric field intensity providing enough kinetic energy for CFs in electric field to penetrate the PDMS adhesive layer, which ensures CFs contact with the interdigital electrode to form a galvanic circle and fixes the short carbon fibers to the PI substrate. Further, micro-computed tomography (micro-CT) was used to analyze area density of CFs: as the fiber length decreases, the number of fibers per unit area (Figure 2c) decreases gradually.

2.3. The Sensing Characterization and Stability of SCFN Airflow Sensor

In order to explore the sensing performance of SCFN to airflow, the testing device (**Figure 3**a) was established for SCFN airflow sensor under different airflow rates and different angles (see details in the Experimental Section). First, the relative resistance variation in response to airflow at different airflow rates was measured to explore the performance of the airflow sensor, as shown in Figure 3b and Figures S6–S8 in the Supporting Information. The airflow direction was perpendicular to the SCFN airflow sensor; the tube port was around 1 cm from the sensor surface. The slope of resistance variation $(R_0-R)/R_0$ varied with airflow rate was used to define the sensor sensitivity in response to the application of airflow. R_0 and R represent the resistance with no airflow and an airflow is applied, respectively. The values of $\Delta R/R_0$ ($\Delta R = R_0-R$) almost no longer increase when airflow rate is larger than 50 L min^{-1} in our test, hence the sensitivity of airflow range was considered from 1 to 50 L min^{-1}. The SCFN-300 and SCFN-500 sensors show higher sensitivity than SCFN-100. It is worth noting the sensitivity of SCFN-500 decreases when the airflow rate is larger than 30 L min^{-1}. This is probably due to the fact that the sensor with a larger length/diameter ratio has higher fiber areal density (Figure 2c). The overlarge areal density will hinder fiber bending and swinging, and finally decreasing the sensing performance. In the following sections, we chose SCFN-300 with higher sensitivity for further research.

Figure 3c reveals the resistance variation of SCFN-300 is changed at different airflow angle (α = 0°, 45°, 90°, which is defined in Figure 3a). It is expected that the short carbon fibers

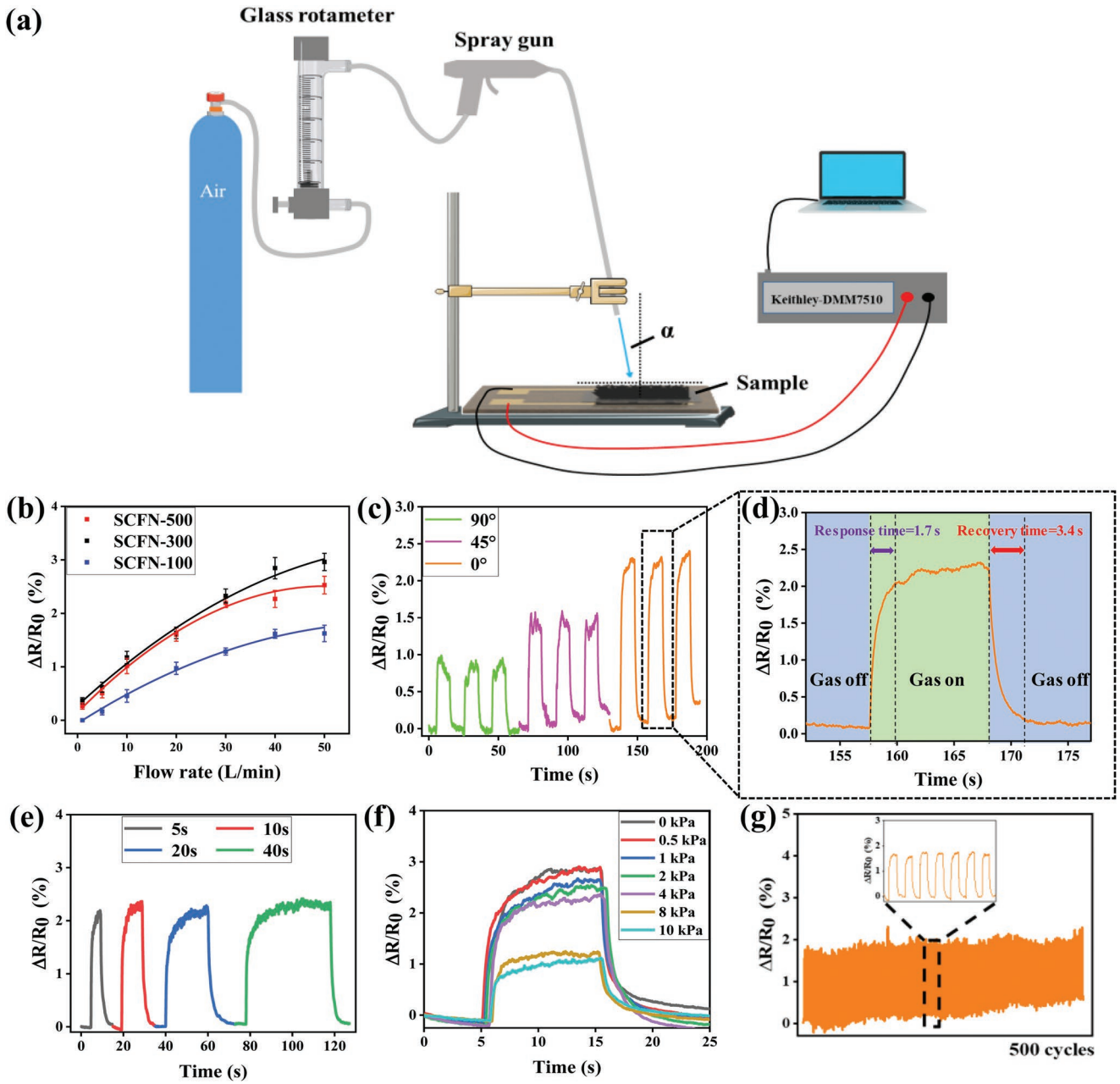

Figure 3. a) Schematic diagram of the setup for the airflow sensing test, α represents the airflow angle inclined from normal direction. b) The resistance variation ($\Delta R/R_0$) against flow rate measured using SCFN-100, SCFN-300, SCFN-500. c) Cyclic sensing curves obtained with the SCFN-300 airflow sensor at an airflow rate of 30 L min^{-1} with different airflow angles. d) The response time and recovery time, which is defined as the time taken to reach a resistance variation of 90% from initial values when the airflow is on or off. e) The response sensing curve of SCFN-300 with different applied time of airflow at 30 L min^{-1}. f) The response sensing curve of SCFN-300 after 20 abrasion resistance test cycle under different stress at a relatively large airflow rate of 50 L min^{-1}. g) The sensing curve of SCFN airflow sensor during 500 airflow on–off cycles at 30 L min^{-1} and 90°.

are able to deform and connect with each other in spite of the air flow angle. The difference, as shown in Figure S9 in the Supporting Information, is that when the airflow direction is perpendicular to the sample surface, the whole fibers can deform, thus resulting in large variation of resistance of the sensor; however, when the airflow direction is parallel to the sample surface, only part of fibers facing the airflow can deform, the fibers are not fully deformed, therefore, the resistance variation becomes smaller. When the airflow angle is between 0° and 90°, the resistance variation is between the values of perpendicular and parallel directions, and the smaller the value of α, the closer to the perpendicular direction.

Figure 3d exhibits the signal changes if airflow is on or off. When an airflow is applied to the SCFN sensor, a signal is gotten seen from the curve, if the airflow is off, then the curve recovers to the initial state. Thus, the response and

recovery times are defined as the time from airflow on/off to 90% increase/decrease in $\Delta R/R_0$. The response and recovery times are 1.7 and 3.4 s for SCFN-300 applied (α = 0°) at 30 L min^{-1}. Further investigations on the response and recovery times at different airflow rate are shown in Figure S10a in the Supporting Information (average response and recovery times are 1.68 and 3.51 s, respectively). The fast change of contact resistance makes SCFN airflow sensor reveal fast response and recovery ability. Table S1 in the Supporting Information compares the detection range and response time of our work with previously reported works. Most of the airflow sensors reported cannot possess both low detection limit and fast response time simultaneously, e.g., a CSF@CNTs airflow sensor[50] possesses a response time of 0.021 s, but its detection limit is 0.11 m s^{-1}. A reduced graphene oxide[11] sensor has been prepared with ultralow detection limit (0.026 m s^{-1}), however, its response time is relatively long (26 s).

Good reliability and stability are important for airflow sensors. Figure 3e suggests a stable and periodic curve, and there is no obvious change for response and recovery times when airflow was applied to SCFN-300 at 30 L min^{-1} for 5, 10, 20, and 40 s (Figure S10b, Supporting Information). It shows that the SCFN airflow sensor is not sensitive to the time of blowing, and still shows reliability. The wear abrasion of sensor is also important to real application. Here, the sensing performance of SCFN-300 was investigated after 20 cycles of abrasion resistance (Figure S11, Supporting Information) under different applied stresses. As shown in Figure 3f, SCFN-300 still reveals obvious signal peaks even after 10 kPa, even though the variation of $\Delta R/R_0$ decreases. Excessive applied stress may result in changed orientation of fibers or fiber pullout and even breakage. In spite of that our sensor still resists a certain degree of pressing, which is an obvious advantage over other hair-like airflow sensors. Also, the performance of SCFN airflow sensor is investigated during/after bending, as shown in Figure S12 in the Supporting Information, there is no obvious change in $\Delta R/R_0$, which means bending does not affect performance of SCFN airflow sensor obviously. Furthermore, cyclic signals during 500 consecutives on/off of airflow are shown in Figure 3g, which indicate the excellent stability and reliability of SCFN airflow sensor in long-term use.

2.4. The Airflow Sensing Mechanism Exploration

Figure 4a illustrates the schematic diagram of how the SCFN airflow sensor works under airflow. The short fibers, like filiform hairs of insects, can deform under the application of airflow, form network structure. As a voltage is applied to the sensor, the current can pass through the network (Figure 4b). There are two paths for current to flow in SCFN sensor: flowing through the PDMS "skin" or short carbon fibers network. As a result, the equivalent circuit diagram of SCFN structure is established based on the current flow model, as shown in Figure 4c. When current flows through the network structure, the current flows vertically upward first, passing the resistance through thickness direction (R_t), and then through network

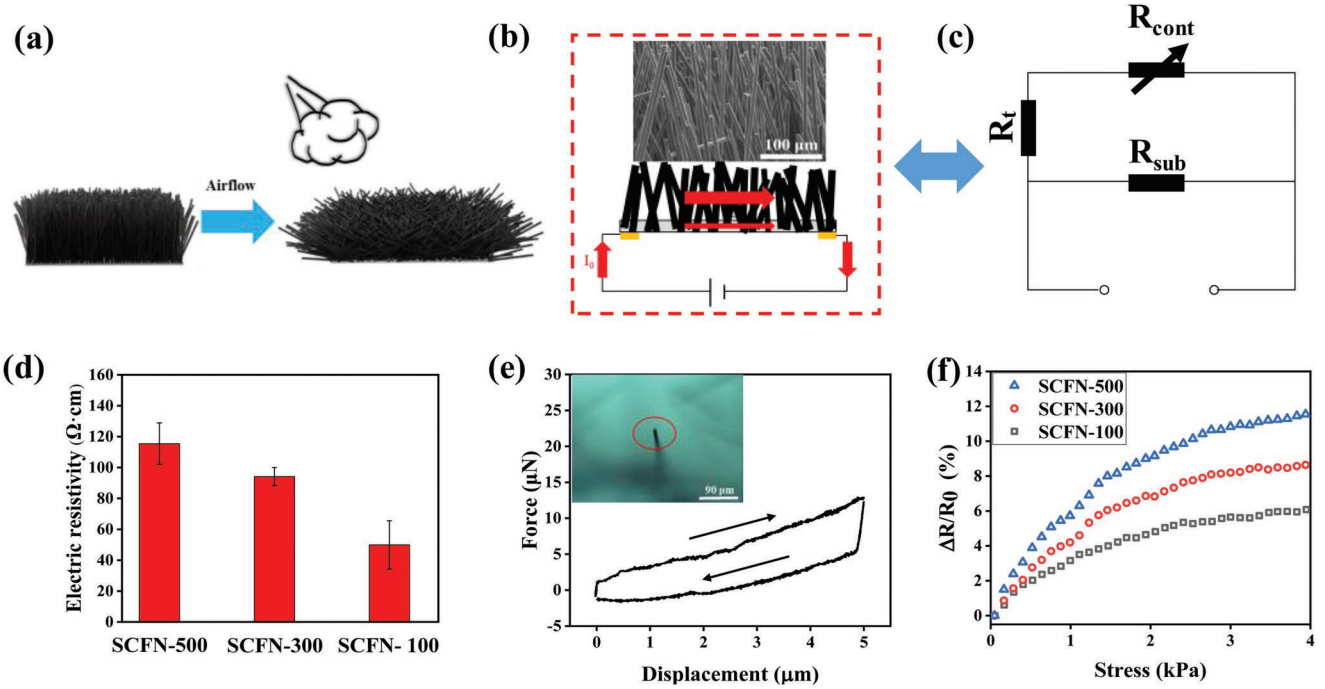

Figure 4. a) Schematic diagram illustrating the change of carbon fiber network structure during airflow. b) The current direction of SCFN airflow sensor (SEM microstructure of SCFN is also shown above). c) An equivalent circuit diagram of SCFN airflow sensor (R_t, R_{cont}, R_{sub} represent the resistance through thickness direction of SCFN and contact resistance of SCFN in-plane direction and the resistance of substrate). d) The resistance values of SCFN-100, SCFN-300, SCFN-500. e) Force–displacement curve of a flocked single carbon fiber (≈500 μm long, average orientation angle is 77°) tested using diamond tip. f) The resistance variation ($\Delta R/R_0$) against direct-contact stress of SCFN airflow sensors tested by DMTA.

structure. We labeled the resistance of network in plane direction as R_{cont}, and the resistance of PDMS layer as R_{sub}. Then the total resistance of SCFN (R) can be calculated as following equation

$$R = \frac{1}{\frac{1}{R_{sub}} + \frac{1}{R_t + R_{cont}}} = \frac{1}{1 + \left(\frac{R_t + R_{cont}}{R_{sub}}\right)} \cdot (R_t + R_{cont}) \quad (1)$$

R_{sub} is much larger than $R_t + R_{cont}$ due to the PDMS adhesive layer is almost nonconductive, therefore, $R \approx R_t + R_{cont}$ according to Equation (1). In general, mechanical deformation of SCFN structure occurs when an airflow is applied on SCFN airflow sensor, increasing contact sites of CFs, as a result, R_{cont} decreases, while R_t and R_{sub} are almost changeless (the value of R_t is close to the bulk resistance of CFs). Therefore, the airflow signal is converted into a mechanical signal when the fiber network structure is deformed, and then converted into an electrical signal through the change of contact resistance, so as to realize sensing of airflow. In addition, the poorly oriented SCFN possesses lower resistance (Figure 4d), namely, more contact sites, which is easier to reach saturation of contact sites, that is why SCFN-100 possesses lower sensitivity.

To further experimentally demonstrate the fiber response to weak force, we used diamond nanoindenter tip to touch a single carbon fiber (Figure S13 in the Supporting Information, ≈500 µm long, orientation angle ≈77°), which was flocked on a transparent glass substrate with PDMS adhesive layer. The displacement control mode was used to move needle tip down for 5 µm after touching the fiber. As a comparison, PDMS "skin" was also tested (Figure S14a, Supporting Information). The maximum force for PDMS is much larger than for single carbon fiber (see Figure S14a in the Supporting Information and Figure 4e). Note if the needle tip does not touch the substrate or the fiber, the sensor would not sense the force, as shown in Figure S14b in the Supporting Information. As shown in Figure 4e, the curves change linearly when force is applied to the top of CF, the response behavior of the fibers is similar to that of a cantilever beam constrained by an angular spring on the fixed end, it only takes a few micro-Newtons of force to drive a single carbon fiber. The arrows in Figure 4e represent the process of loading and unloading forces, showing repeatability of loading and unloading cycles. This result verifies that the hair-like fibers on flexible "skin" are easy to deform under tiny force (several micro-Newtons). Furthermore, a dynamic mechanical thermal analyzer (DMTA) was used to press the SCFN samples from the *Z*-direction (Figure S15, Supporting Information); here, small stress is applied (Figure S16, Supporting Information). Figure 4f reveals that the resistance change value of SCFN sample increases with the application of force from thickness direction. Deformation due to direct contact also caused increasing of contact points between the fibers, resulting in a resistance change. These prove experimentally that tiny forces make the fibers to bend and swing, causing network structure to deform, and then the contact resistance would change. This provides unique structural characteristics for airflow sensing.

2.5. Applications of the SCFN Airflow Sensor

The sensing performance of single SCFN airflow sensor was elaborated above, then we used the designability of SCFN sensor to demonstrate its potential application further. In a real situation, more complicated and diverse functions can be realized through the combination of several SCFN airflow sensor units. Four SCFN-300 airflow sensors were adhered to the four surfaces of a toy due to the flexible and adhesive characteristics of the sensor, as shown in **Figure 5**a,b. When an airflow is applied from a direction perpendicular to sensor 1, the response signals of the four sensors are shown in Figure 5c–f, respectively. Sensor 1 reveals a highest variation of $\Delta R/R_0$, sensor 2 and sensor 3 come second, while sensor 4 reveals almost no signals. Thus, it was concluded that the airflow is from direction 1, and the flow-rate is around 20 L min^{-1}. The accuracy of velocity and direction measurement might be improved by increasing the number of sensor units and combining proper algorithms.

In industrial production or even international space station, the gas leakage is an intractable problem, which may bring about serious accident. Detection of weak gas leakage is a big challenge. With ultrasensitivity to weak airflow, the SCFN airflow sensor may play the essential role in this area. A simplified illustration is shown in **Figure 6**a. Nitrogen gas was injected into a sealed reaction device that requires gas protection, and a small hole was created in advance. Figure 6b shows the related photograph. A probe that based on SCFN-300 airflow sensor was used to detect the gas leakage (Video S4, Supporting Information). There is no signal variation on the screen, as the probe is far away from the gas leak location (Figure 6c,f); as the probe is close enough to the gas leak location, a signal variation appears on the screen in a short time (Figure 6d,g); once the probe is moved away, the signal was recovered to the initial level (Figure 6e,h). We propose that the SCFN airflow sensor can be mounted between the gap and key position of the complex pipelines to alert the engineers that a gas leak occurs and its accurate location. In addition, we also demonstrate the potential application of our sensor in wearable electronics for sensing movements (Figure S17, Supporting Information). The SCFN sensor can detect the movement of human body and the raising of arm due to the airflow.

3. Conclusions

In summary, inspired by the filiform hair of insects, we fabricated an ultrasensitive and flexible airflow sensor based on SCFN prepared by electrostatic flocking. Short carbon fibers were quasi-vertically oriented in the electric field and fixed by soft PDMS adhesive layer. Similar to filiform hair of insects, the fibers can easily bend and swing, form contacting network microstructure, thus leading to significant variation of contact resistance under weak stress, such as airflow. The forming SCFN airflow sensor revealed ultralow detection limits (0.053 m s^{-1}), wide detection range (0.053–2.66 m s^{-1}), multiangle response (0°–90°) with fast response time (1.7 s). Besides, SCFN airflow sensor also showed excellent stability during airflow on–off cycles and good abrasion resistance. Some demonstrations (3D layout of SCFN airflow sensor to monitoring the velocity and direction of airflow, sensor in wearable electronics for sensing movements, sensor for

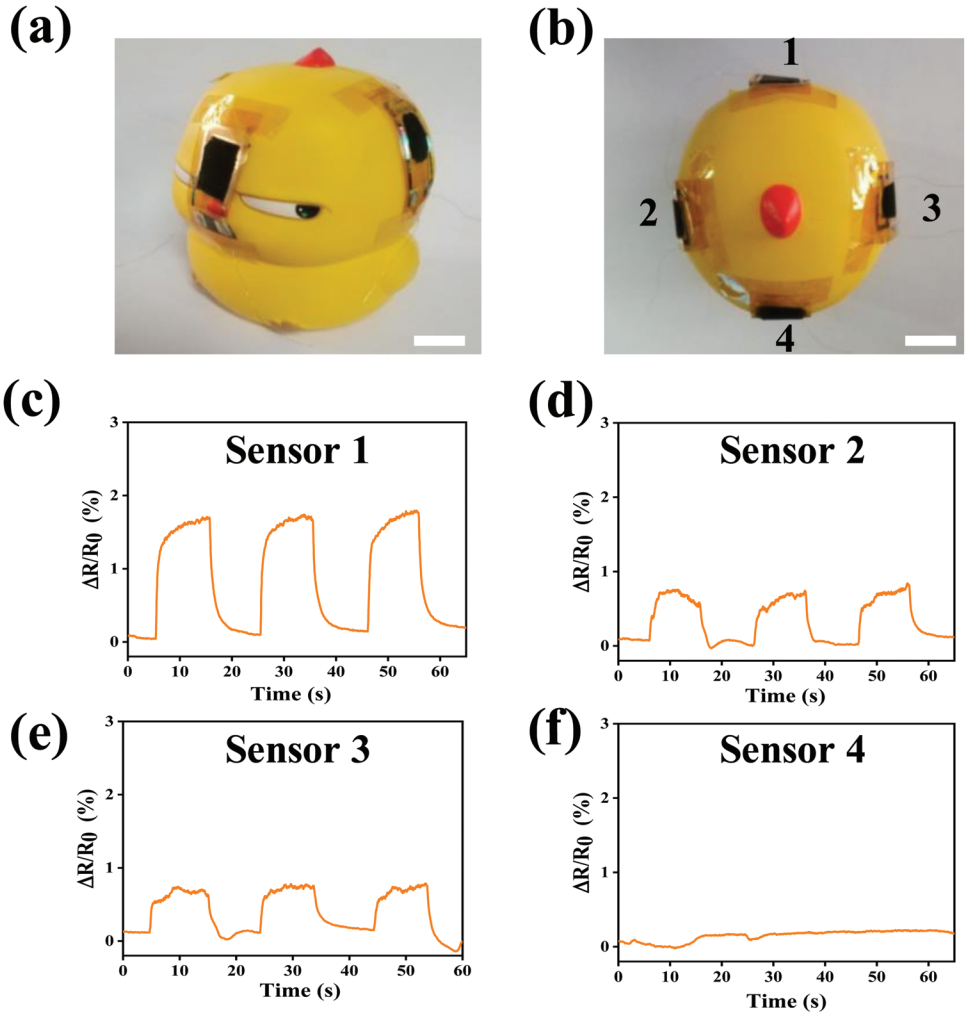

Figure 5. a,b) 3D layout of SCFN airflow sensor (labeled as sensor 1–4) on a toy (scale bar, 1 cm). c–f) The response sensing cycles of sensor 1–4.

detecting of gas leak location for a sealed reaction device) were given to show the potential applications of this SCFN airflow sensor. The high performance, all flexible design, mild and high throughput fabrication endow its potential applications in electronic skin or wearable electronics.

4. Experimental Section

Materials: Polyimide films (Macans) with 10 µm thickness were used for substrates. Continuous polyacrylonitrile-based carbon fibers with 7 µm diameter (Grade T300, Shanghai Liso Composite Co., Ltd.) were chopped and separated with sieves of different mesh numbers (100, 200, 300) so as to get short fibers having different length. PDMS (Sylgard 184) for adhesive layer was purchased from Dow corning Co., Ltd.

Fabrication of Interdigital Electrode: A PI film substrate was first tailored into proper size, and adhered to the metal bracket of a thermal evaporation machine (SBC-2, Beijing KYKY Technology Co., Ltd). Then the PI film was cleaned by acetone for several times. After cleaning, a customized metal mask plate was covered on the PI film and was fixed. At last, metal Cr (10 nm) and Au (100 nm) were, respectively, deposited on it by thermal evaporation.

Fabrication of the Sensor based on SCFN: As shown in schematic diagram of fabrication process in Figure 1a, the precursor and curing agent of PDMS was intensively stirred and degassed using a vacuum deformer (Thinky, Japan) for 5 min. The resulting mixture (precursor/curing agent of PDMS) was used as the flocking adhesive later. Before electrostatic flocking, the short carbon fibers were mechanically vibrated, making them evenly fall onto the bottom plate electrode without any significant agglomeration. The flocking adhesive was applied on PI substrate to cover the interdigital electrode using a wire rod coater to prepare an adhesive layer. Then the substrate was adhered to the upper plate electrode using a double-faced adhesive tape. The separation between the electrodes was set as 10 cm, and the voltage was 30 kV. As the power was on, the short carbon fibers were charged, aligned along the direction of electrical field, flew away from bottom electrode, and inserted to the opposite uncured adhesive layer in 10 s. The sample was put in oven at 80 °C and cured for 120 min.

Characterization: The morphologies and structures of the samples were measured by scanning electron microscopy (SEM, Hitachi, SU8220) and micro-CT (Zeiss, Xradia 510 Versa) with 1.0 µm of voxel resolution. The quasi-static process of fiber swinging process was measured by an optical microscope (Meta Test) in situ observation.

The Test for Driving a Single Carbon Fiber: A very small amount of short carbon fibers was flocked to PDMS adhesive layer on glass substrate. A diamond tip (Berkovich, the radius of tip is 100 nm) of the mechanical testing system for nanoindentation (TI950, Hysitron) equipped with an optical microscope was used to drive a single carbon fiber. In order to ensure that the force was applied to the fiber accurately, the fiber was located through the optical microscope.

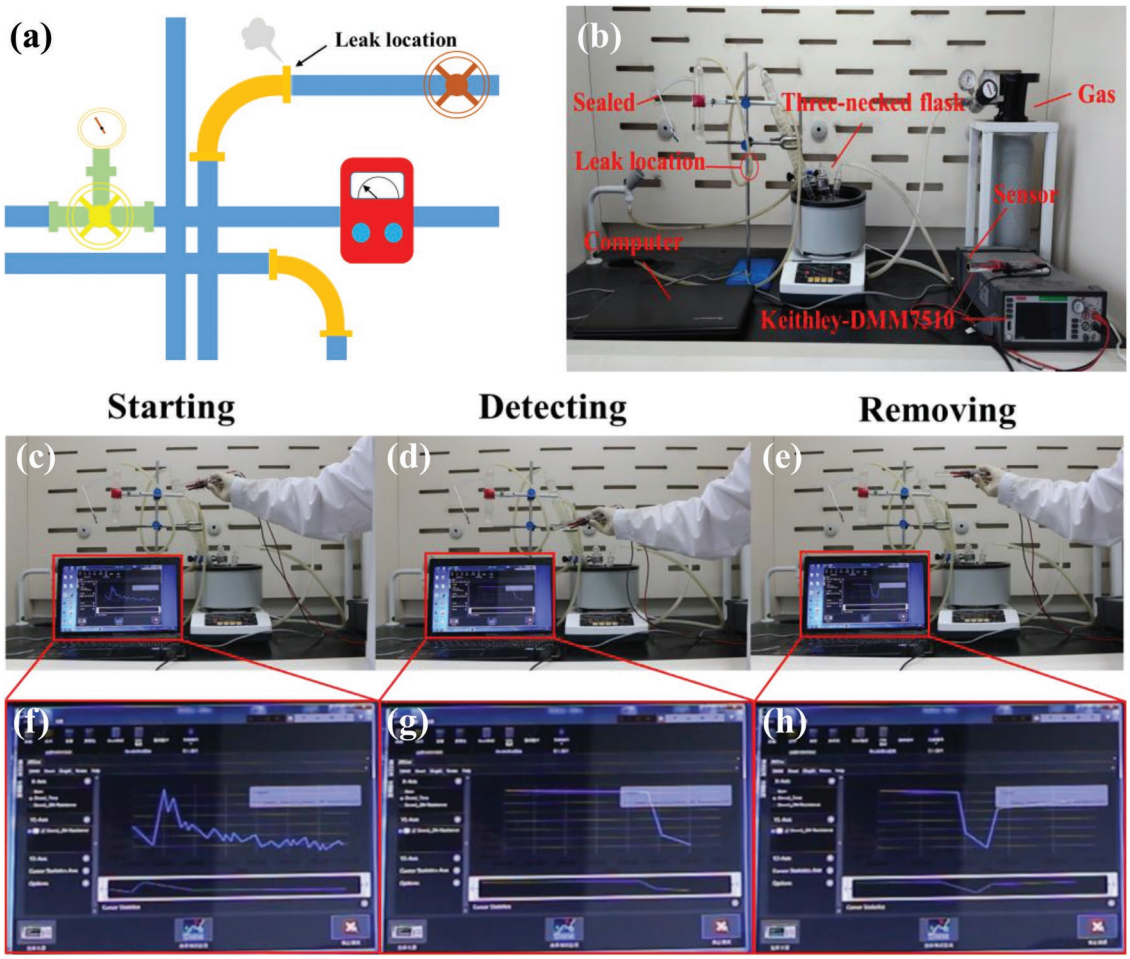

Figure 6. a) Schematic diagram of complex pipeline leakage. b) Optical image of a sealed reaction device, a gas leak was created in advance. c–e) Optical images and f–h) resistance variation curve when detecting the leak location.

Sensing Performance Test of the Sensor: Electrical measuring device of the airflow sensors was set up as shown in Figure 4a. The sensor was fixed on a steel plate, using a glass rotameter to control gas flow and a spray gun to control air flow on or off. A piece of tube was connected with the front of the spray gun and fixed on the iron support to control the angle of air flow, the radius of the tube is 1 cm. The variation of resistance was measured by a computer-controlled digital source meter (Keithley-DMM7510) at room temperature. $(R_0–R)/R_0$ (%) was calculated, where R and R_0 were the resistance of sensor measured when the airflow was on and off, respectively. All tests were carried out in a windless room to avoid interference of air flow. For the data points on same test conditions, the airflow rate (Q) and velocity (v) could be converted by formula: $v = Q/S$, where S is the tube cross-sectional area ($S = \pi r^2$, r is the radius of the tube).

Supporting Information

Supporting Information is available from the Wiley Online Library or from the author.

Acknowledgements

This work was jointly supported by the National Natural Science Foundation of China (grant nos. 51861165103, 11890682, and 11832010), the Austrian-Chinese Cooperative Research and Development Projects (project no.: GJHZ2043), and the Regional Key Projects of the Science and Technology Service Network Program of the Chinese Academy of Sciences (project no.: KFJ-STS-QYZD-121).

Conflict of Interest

The authors declare no conflict of interest.

Data Availability Statement

The data that support the findings of this study are available in the Supporting information of this article.

Keywords

airflow sensing, bioinspired flexible sensor, electrostatic flocking, short carbon fiber network

Received: April 7, 2022
Revised: June 17, 2022
Published online: August 11, 2022

[1] X. Pu, M. Liu, X. Chen, J. Sun, Z. L. Wang, *Sci. Adv.* **2017**, *3*, e1700015.
[2] M. L. Hammock, A. Chortos, B. C. K. Tee, J. B. H. Tok, Z. Bao, *Adv. Mater.* **2013**, *25*, 5997.
[3] J. Chen, Y. Zhu, X. Chang, D. Pan, G. Song, Z. Guo, N. Naik, *Adv. Funct. Mater.* **2021**, *31*, 2104686.
[4] B. Peng, F. Zhao, J. Ping, Y. Ying, *Small* **2020**, *16*, 2002681.
[5] A. Talbi, L. Gimeno, J. Gerbedoen, R. Viard, A. Soltani, V. Mortet, V. Preobrazhensky, A. Merlen, P. Pernod, *J. Micromech. Microeng.* **2015**, *25*, 125029.
[6] F. Xing, G.-X. Meng, Q. Zhang, L.-T. Pan, P. Wang, Z.-B. Liu, W.-S. Jiang, Y. Chen, J.-G. Tian, *Nano Lett.* **2014**, *14*, 3563.
[7] K.-H. Kim, S. K. Hong, N.-S. Jang, S.-H. Ha, H. W. Lee, J.-M. Kim, *ACS Appl. Mater. Interfaces* **2017**, *9*, 17499.
[8] Y. Joo, J. Yoon, J. Ha, T. Kim, S. Lee, B. Lee, C. Pang, Y. Hong, *Adv. Electron. Mater.* **2017**, *3*, 1600455.
[9] G. Y. Bae, S. W. Pak, D. Kim, G. Lee, D. H. Kim, Y. Chung, K. Cho, *Adv. Mater.* **2016**, *28*, 5300.
[10] X. Wang, Y. Gu, Z. Xiong, Z. Cui, T. Zhang, *Adv. Mater.* **2014**, *26*, 1336.
[11] J. Park, Y. Lee, J. Hong, M. Ha, Y. D. Jung, H. Lim, S. Y. Kim, H. Ko, *ACS Nano* **2014**, *8*, 4689.
[12] S. C. Mannsfeld, B. C. Tee, R. M. Stoltenberg, C. V. H. Chen, S. Barman, B. V. Muir, A. N. Sokolov, C. Reese, Z. Bao, *Nat. Mater.* **2010**, *9*, 859.
[13] B. Liang, W. Chen, Z. He, R. Yang, Z. Lin, H. Du, Y. Shang, A. Cao, Z. Tang, X. Gui, *Small* **2017**, *13*, 1702422.
[14] W. Liu, N. Liu, Y. Yue, J. Rao, F. Cheng, J. Su, Z. Liu, Y. Gao, *Small* **2018**, *14*, 1704149.
[15] G. Ge, Y. Lu, X. Qu, W. Zhao, Y. Ren, W. Wang, Q. Wang, W. Huang, X. Dong, *ACS Nano* **2019**, *14*, 218.
[16] M. Soni, M. Bhattacharjee, M. Ntagios, R. Dahiya, *IEEE Sens. J.* **2020**, *20*, 7525.
[17] M. Sadeghi, R. Peterson, K. Najafi, *J. Micromech. Microeng.* **2013**, *23*, 085017.
[18] H. Guo, J. Chen, L. Tian, Q. Leng, Y. Xi, C. Hu, *ACS Appl. Mater. Interfaces* **2014**, *6*, 17184.
[19] A. Talbi, L. Gimeno, J. C. Gerbedoen, R. Viard, A. Soltani, V. Mortet, V. Preobrazhensky, A. Merlen, P. Pernod, *J. Micromech. Microeng.* **2015**, *25*, 125029.
[20] W. Zhou, P. Xiao, Y. Liang, Q. Wang, D. Liu, Q. Yang, J. Chen, Y. Nie, S. W. Kuo, T. Chen, *Adv. Funct. Mater.* **2021**, *31*, 2105323.
[21] H. Wang, S. Li, Y. Wang, H. Wang, X. Shen, M. Zhang, H. Lu, M. He, Y. Zhang, *Adv. Mater.* **2020**, *32*, 1908214.
[22] Z. Xu, K. Wu, S. Zhang, Y. Meng, H. Li, L. Li, *Mater. Horiz.* **2017**, *4*, 383.
[23] X. Shuai, P. Zhu, W. Zeng, Y. Hu, X. Liang, Y. Zhang, R. Sun, C.-p. Wong, *ACS Appl. Mater. Interfaces* **2017**, *9*, 26314.
[24] T. Jiang, L. Deng, W. Qiu, J. Liang, Y. Wu, Z. Shao, D. Wang, M. Zhang, X. Qian, J. Zhong, *Biosens. Bioelectron.* **2020**, *163*, 112288.
[25] D. Maier, E. Laubender, A. Basavanna, S. Schumann, F. Güder, G. A. Urban, C. Dincer, *ACS Sens.* **2019**, *4*, 2945.
[26] R. Cao, J. Wang, S. Zhao, W. Yang, Z. Yuan, Y. Yin, X. Du, N.-W. Li, X. Zhang, X. Li, Z. L. Wang, C. Li, *Nano Res.* **2018**, *11*, 3771.
[27] R.-H. Ma, Y.-H. Wang, C.-Y. Lee, *Sensors* **2011**, *11*, 2715.
[28] H. H. Yan, Y. Rahayu, in *Proc. Int. Conf. on Electrical Engineering Computer Science and Informatics*, IEEE, Piscataway, NJ, **2014**, pp. 207–212.
[29] A. G. P. Kottapalli, M. Bora, M. Asadnia, J. Miao, S. S. Venkatraman, M. Triantafyllou, *Sci. Rep.* **2016**, *6*, 19336.
[30] Y.-F. Liu, P. Huang, Y.-Q. Li, Q. Liu, J.-K. Tao, D.-J. Xiong, N. Hu, C. Yan, H. Wang, S.-Y. Fu, *J. Mater. Chem. A* **2019**, *7*, 1889.
[31] N. Izadi, M. J. de Boer, J. W. Berenschot, G. J. Krijnen, *J. Micromech. Microeng.* **2010**, *20*, 085041.
[32] Y. Cao, Y. J. Tan, S. Li, W. W. Lee, H. Guo, Y. Cai, C. Wang, B. C. K. Tee, *Nat. Electron.* **2019**, *2*, 75.
[33] H. Liu, S. Zhang, R. Kathiresan, T. Kobayashi, C. Lee, *Appl. Phys. Lett.* **2012**, *100*, 223905.
[34] Y. Bian, R. Liu, S. Hui, *Funct. Mater. Lett.* **2016**, *09*, 1650001.
[35] Y. Bian, Y. Zhang, X. Xia, *J. Bionic Eng.* **2016**, *13*, 416.
[36] J. Paek, J. Kim, *Nat. Commun.* **2014**, *5*, 3324.
[37] F. Xing, Y. Yang, J. Shen, W. Jiang, Z. Liu, S. Zhu, X. Yuan, *Sens. Actuators, B* **2016**, *235*, 474.
[38] J. Zhang, L. Hao, F. Yang, W. Jiao, W. Liu, Y. Li, R. Wang, X. He, *ACS Appl. Mater. Interfaces* **2016**, *8*, 33848.
[39] Y. Liu, L. Zhao, R. Avila, C. Yiu, T. Wong, Y. Chan, K. Yao, D. Li, Y. Zhang, W. Li, *Mater. Today Phys.* **2020**, *13*, 100199.
[40] Y. Lee, J. Park, A. Choe, S. Cho, J. Kim, H. Ko, *Adv. Funct. Mater.* **2020**, *30*, 1904523.
[41] P. Zhu, H. Du, X. Hou, P. Lu, L. Wang, J. Huang, N. Bai, Z. Wu, N. X. Fang, C. F. Guo, *Nat. Commun.* **2021**, *12*, 4731.
[42] Y. Zhao, W. Gao, K. Dai, S. Wang, Z. Yuan, J. Li, W. Zhai, G. Zheng, C. Pan, C. Liu, *Adv. Mater.* **2021**, *33*, 2102332.
[43] B. C. Tee, C. Wang, R. Allen, Z. Bao, *Nat. Nanotechnol.* **2012**, *7*, 825.
[44] E. Tauber, J. Camhi, *J. Exp. Biol.* **1995**, *198*, 1895.
[45] F. Barth, *Naturwissenschaften* **2000**, *87*, 51.
[46] C. Klopsch, H. C. Kuhlmann, F. G. Barth, *J. R. Soc., Interface* **2012**, *9*, 2591.
[47] M. E. McConney, C. F. Schaber, M. D. Julian, W. C. Eberhardt, J. A. Humphrey, F. G. Barth, V. V. Tsukruk, *J. R. Soc., Interface* **2009**, *6*, 681.
[48] R. Kerekes, C. Schell, *J. Pulp Pap. Sci.* **1992**, *18*, J32.
[49] K. Uetani, S. Ata, S. Tomonoh, T. Yamada, M. Yumura, K. Hata, *Adv. Mater.* **2015**, *26*, 5857.
[50] Q. Jiang, R. Li, F. Wang, X. Shi, F. Chen, Y. Huang, B. Wang, W. Zhang, X. Wu, F. Wei, *Adv. Mater.* **2022**, *34*, 2107062.